waveform was the Welti sequence owing to the pseudorandom nature of the envelope detector output.

The square-law detector performed similarly for both waveforms because energies were kept equal. It also was the most effective detector compared with the other receivers. The least sensitive receiver was the wideband receiver. The requirement to open the bandwidth allows the noise level to increase requiring higher pulse energies for detection. The Welti waveform showed approximately a $4:1$ reduction in range of detection for the channelized receiver while not showing an appreciable improvement in the square-law or delay and multiply receivers. The Welti waveform is less detectable in all receivers but offers the greatest advantage in defeating the channelized receiver.

FRANK B. GROSS
Dept. of Electrical Engineering
FAMU-FSU College of Engineering
2525 Pottsdamer St.
Tallahassee, FL 321310
E-mail: (gross@eng.fsu.edu)

KENNY CHEN
RCC Consultants, Inc.
Tallahassee, FL 32303

REFERENCES

[1] Wiley, R. G.
Electronic Intelligence: The Interception of Radar Signals.
Norwood, MA: Artech House, 1985.

[2] Schleher, D. C.
Low probability of intercept radar.
In *Record of the IEEE International Radar Conference*, 1985, 346–349.

[3] Schrick, G., and Wiley, R. G.
Interception of LPI radar signals.
In *Record of the IEEE International Radar Conference*, Arlington, VA, May 7–10, 1990, 108–111.

[4] Ruffe, L. I., and Stott, G. F.
LPI considerations for surveillance radars.
In *Proceedings of the International Radar Conference*, Brighton, UK, 1992, 200–202.

[5] Pace, P.
Detecting and Classifying Low Probability of Intercept Radar.
Norwood, MA: Artech House, 2004.

[6] Milne, P. R., and Pace, P. E.
Wigner distribution detection and analysis of FMCW and P-R polyphase LPI waveforms.
In *Proceedings of IEEE International Conference on Acoustics, Speech, and Signal Processing* (ICASSP '02), *Vol. 4*, May 13–17, 2002.

[7] Weeks, G. D., Townsend, J. K., and Freebersyser, J. A.
A method and metric for quantitatively defining low probability of detection.
IEEE Military Communication Conference Proceedings, Vol. 3, (Oct. 1998), 821–826.

[8] Welti, G. R.
Quarternary codes for pulsed radar.
IRE Transactions on Information Theory, **IT-6** (June 1960), 400–408.

[9] Dixon, R.
Spread Spectrum Systems with Commercial Applications (3rd ed).
New York: Wiley, 1994, 18.

[10] Schleher, C.
Introduction to Electronic Warfare.
Norwood, MA: Artech house, 1986.

[11] Helstrom, C.
Elements of Signal Detection and Estimation.
Englewood Cliffs, NJ: Prentice-Hall, 1995, 46.

[12] Skolnik, M.
Introduction to Radar Systems.
New York: McGraw-Hill, 1980, 26.

Robust Estimation of Radar Reflectivities in Multibaseline InSAR

We examine how to reliably exploit baseline diversity of a multichannel interferometric synthetic aperture radar (InSAR) system to overcome the layover problem. In practice, the baseline steering vectors will be imprecise, resulting in array miscalibration. We propose a nonparametric multilook approach based on robust Capon beamforming (RCB), allowing for uncertainty in the steering vectors.

I. INTRODUCTION

Interferometric synthetic aperture radar (InSAR) is a powerful and increasingly expanding technique allowing estimation of three-dimensional terrain images, with high spatial resolution and height accuracy. Typically, a (single-baseline) InSAR system acquires two complex SAR images from two antennas slightly separated by a (single) cross-track baseline [1, 2]. Using the phase difference between the echoes collected by the two antennas of the interferometer, the so-called interferometric phase φ, one can accurately determine the elevation angle θ and as a result the terrain height for each pixel corresponding to the same area of ground in both images. Unfortunately, the technique suffers from the layover phenomenon that shows up when the imaged scene contains highly sloping areas or discontinuous surfaces [1, 2]; see also Fig. 1. In these conditions, the received signal is the superposition of the echoes backscattered from the various patches of terrain that are mapped in the same range-azimuth resolution cell but have different elevation angles [2]. The

Manuscript received February 17, 2004; revised October 4 and November 26, 2004; released for publication December 6, 2004.

IEEE Log No. T-AES/41/2/849050.

Refereeing of this contribution was handled by E. S. Chornoboy.

This work was partially supported by the Italian National Research Council (CNR).

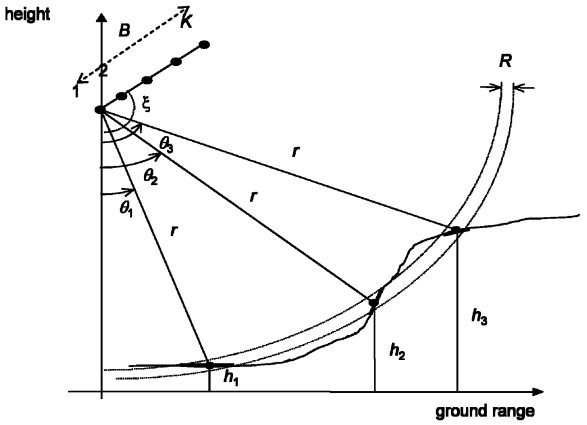

Fig. 1. Geometry of interferometric system in presence of layover (example with 3 layover sources); r is slant range, R is slant range resolution.

result is that the height map produced by the InSAR system is affected by strong distortions, i.e., severe bias and inflated variance. A multibaseline InSAR system has the ability to resolve the multiple sources along the elevation angle, and several approaches has been suggested in the literature [3–8]. In [3], a beamforming approach was suggested to solve this problem. However, beamforming suffers from well-known problems of resolution and leakage, and generally, it is not possible to obtain a large overall baseline with enough coherent samples to attain the desired resolution in elevation [9]. Subsequently, superresolution techniques were also considered [4, 6, 10]. An additional problem is the fact that the backscattering sources cannot be represented as point-like targets, because of their extended nature [1, 2]. The backscattered signal is affected by the so-called speckle phenomenon, which can be well modeled as a complex-valued multiplicative stochastic process. To counteract the deleterious effects of the speckle, it is often advantageous to process more than one look data, combining several observations of the same terrain area [1]. This was done in [11], where the APES algorithm was extended to handle multilook data, and in [12], where the Capon, least-squares, root-MUSIC, and RELAX algorithms were applied to the multibaseline problem. As is well known, the data-dependent Capon and APES methods have better resolution and much better interference rejection capability than the standard data-independent beamformer, provided that the array steering vector corresponding to the signal of interest is accurately known. However, if the steering vectors are uncertain, which due to array calibration errors is the typical situation in practice, the performance of the Capon beamformer may become worse than that of the standard beamformer (see, e.g., [13]). The subject of this work is the estimation of radar reflectivities of the multiple backscattering sources by processing independent looks of the multibaseline InSAR signal under the assumption that the spatial sampling of the baseline is slightly nonuniform due to limited accuracy in the positioning instruments measuring the actual flight path, as well as calibration errors of the array. Accurate measurements of the radar reflectivities are often of interest, e.g., for vegetation and snow mapping, land-use monitoring, soil moisture determination, and forestry [14, 15]. Typically, some form of prior knowledge of the interferometric phases is needed to enable estimation of the reflectivities; herein, we make no such assumptions but rather treat the interferometric phases as unknown nuisance parameters that are jointly estimated with the textures. To enable this estimation under slight nonuniform conditions, we apply the robust Capon beamformer (RCB) recently proposed by Stoica et al. [16, 17]. The most relevant difference between [16] and [17] and our work is that in [16] and [17] the amplitudes are assumed to be the same for each look, while in our formulation they are different due to the multiplicative noise. Thus, the novel contribution in this work relies mainly on the application of the RCB to the multicomponent multibaseline InSAR signal, introducing an array error model for this specific application and extending the robust approach to the least squares estimator of the signal amplitudes. The rest of this paper is organized as follows. The data model, the array error model, and the estimation problem are stated in Section II. The multilook standard Capon beamformer (MSCB) is reviewed in Section III, and the suggested multilook robust Capon beamformer (MRCB) is presented in Section IV. Simulation results are described in Section V, and conclusions are reported in Section VI.

II. MODEL DESCRIPTION

Consider a multibaseline cross-track interferometer system with K two-way phase centers aligned to form an array [6, 12, 15]. The distance between the first and last phase center in the array represents the overall baseline length B, as shown in Fig. 1. To increase the accuracy in presence of speckle, multiple looks are collected from homogeneous adjacent pixels or from multiple observations obtained by partitioning the synthetic aperture [1, 2]. Typically, a very limited number of looks N is available. The complex amplitudes of the pixels of the nth look corresponding to the same imaged area on the ground, collected at the K phase centers of the antenna array in the presence of layover, are modeled as

$$\mathbf{y}(n) = \sum_{m=1}^{N_s} \sqrt{\tau_m}\mathbf{x}_m(n) \odot \mathbf{a}(\varphi_m) + \mathbf{v}(n) \tag{1}$$

for $n = 1,\ldots,N$, where $\mathbf{y}(n)$, $\mathbf{x}_m(n)$, $\mathbf{a}(\varphi_m)$, and $\mathbf{v}(n)$ are K-dimensional complex vectors, $\odot$ is the Schur-Hadamard (elementwise) product, and N_s

is the number of extended backscattering sources, i.e., the number of laid over terrain patches located in the same range-azimuth resolution cell, having different elevations. We assume here that N_s is known, noting that different methods to estimate N_s have been discussed in [18] and [19]. The parameter τ_m is real-valued and positive and denotes the mean pixel intensity contribution from the mth patch; it is assumed not to change from one look to the other, but to be source dependent. This parameter is the texture, or radar reflectivity, and can be regarded as a scaled normalized radar cross section [14]. As in [6], we consider the reflectivities as deterministic unknown parameters. Further, the interferometric phases $\{\varphi_m\}$ are defined as the phase difference between the two furthest phase centers. They are related in a one-to-one mapping with the elevation angle of the mth terrain patch θ_m and to the spatial frequency ω_m as

$$\varphi_m = (K-1)\omega_m = 4\pi\lambda^{-1}B\cos(\xi-\theta_m) \tag{2}$$

with λ denoting the radar wavelength and ξ the baseline tilt [1, 12]. From knowledge of the imaging system geometry and of the interferometric phases, we can retrieve the heights $\{h_m\}_{m=1}^{N_s}$ and produce both undistorted height maps of the land surface [1], and undistorted reflectivity maps [15]. Following [16], we allow for calibration errors in the array steering vector $\mathbf{a}(\varphi)$. More specifically, we assume that the only knowledge we have about the steering vector is that it belongs to the following uncertainty ellipsoid

$$\mathbf{e}_a^H(\varphi)\mathbf{C}^{-1}\mathbf{e}_a(\varphi) \le 1 \tag{3}$$

where $(\cdot)^H$ denotes the conjugate transpose and $\mathbf{e}_a$ is the steering vector error,

$$\mathbf{e}_a(\varphi) = \mathbf{a}(\varphi) - \bar{\mathbf{a}}(\varphi). \tag{4}$$

Here, $\bar{\mathbf{a}}(\varphi)$ is the steering vector of the perfectly calibrated array. Without loss of generality, we assume the array to be a uniform linear array; under the far field assumption, $\bar{\mathbf{a}}$ can be written as

$$\bar{\mathbf{a}}(\varphi) = [1 \quad e^{j\varphi/(K-1)} \quad \dots \quad e^{j\varphi}]^{\mathrm{T}} \tag{5}$$

where $(\cdot)^{\mathrm{T}}$ denotes the transpose. The positive definite matrix $\mathbf{C}$ in (3) determines the size and shape of the uncertainty ellipsoid. Let $\mathbf{e}_{i\|B}$ and $\mathbf{e}_{i\perp B}$ be the ith sensor misplacement in the parallel baseline and in the orthogonal baseline directions, respectively. Operations around $\varphi \approx 0$ are typical as the interferometric array usually faces the imaged scene (typically, we reconduct to this situation by means of signal deramping); thus it is reasonable to expect the transverse errors $\mathbf{e}_{i\perp B}$ to produce errors in the phases at the various phase centers which are zero to first order, while the frontal errors $\mathbf{e}_{i\|B}$ produce noninfinitesimal errors in the phases at various array phase centers. To simplify notation, we introduce the normalized transverse and frontal errors,

$$\tilde{\mathbf{e}}_{i\perp B} = \mathbf{e}_{i\perp B}/B \tag{6}$$

$$\tilde{\mathbf{e}}_{i\|B} = \mathbf{e}_{i\|B}/\lambda. \tag{7}$$

For a scene facing the array, the ith steering vector element can be approximated as

$$[\mathbf{a}(\varphi)]_i \approx e^{j\left((i-1/K-1)+\tilde{\mathbf{e}}_{i\perp B}\right)\varphi} e^{j4\pi\tilde{\mathbf{e}}_{i\|B}} \tag{8}$$

which, using a first-order Taylor expansion of the perturbation components (dropping the second-order terms) assuming $\varphi \approx 0$, yields

$$[\mathbf{a}(\varphi)]_i \approx e^{j(i-1/K-1)\varphi}(1 + j\varphi\tilde{\mathbf{e}}_{i\perp B} + j4\pi\tilde{\mathbf{e}}_{i\|B}) \tag{9}$$

and thus

$$[\mathbf{e}_a(\varphi)]_i \approx e^{j(i-1/K-1)\varphi}(j\varphi\tilde{\mathbf{e}}_{i\perp B} + j4\pi\tilde{\mathbf{e}}_{i\|B}). \tag{10}$$

Assuming uncorrelated transverse and frontal error, we get

$$\mathrm{var}\{[\mathbf{e}_a(\varphi)]_i\} = \varphi^2\sigma_{i\perp B}^2 + (4\pi)^2\sigma_{i\|B}^2 \tag{11}$$

where $\sigma_{i\perp B}^2 = \mathrm{var}\{\tilde{\mathbf{e}}_{i\perp B}\}$ and $\sigma_{i\|B}^2 = \mathrm{var}\{\tilde{\mathbf{e}}_{i\|B}\}$. This variance is lower bounded by the worst case value

$$\mathrm{var}_{\max}\{[\mathbf{e}_a(\varphi)]_i\} = \varphi_{\max}^2\sigma_{i\perp B}^2 + 16\pi^2\sigma_{i\|B}^2 \tag{12}$$

where $\varphi_{\max}$ is the maximum absolute value of φ that can be encountered during the interferometric operation. The worst case variance can be used as a rule of thumb to quantify the uncertainty ellipsoid $\mathbf{C}$, i.e., $\mathbf{C} = E\{\mathbf{e}_a(\varphi)\mathbf{e}_a^H(\varphi)\}$, where $\mathrm{E}\{\cdot\}$ denotes the expectation operator. Thus, the diagonal elements of $\mathbf{C}$ can be well modeled using $\mathrm{var}_{\max}\{[\mathbf{e}_a(\varphi)]_i\}$, evaluated from given values of $\sigma_{i\perp B}^2$ and $\sigma_{i\|B}^2$ for the interferometric application at hand. Depending of the desired accuracy/complexity, the off-diagonal terms in $\mathbf{C}$ may be set to zero, or evaluated as $\mathrm{cov}\{[\mathbf{e}_a(\varphi)]_i, [\mathbf{e}_a(\varphi)]_l\}$, derived in a similar procedure as above. Further, the speckle vectors in (1), $\{\mathbf{x}_m(n)\}$, are modeled as stationary complex Gaussian distributed vectors with zero-mean, unit variance, and covariance matrix

$$\mathbf{Q}_m = \mathrm{E}\{\mathbf{x}_m(n)\mathbf{x}_m^H(n)\}, \qquad m = 1,\dots,N_s. \tag{13}$$

In shorthand notation, we write $\mathbf{x}_m(n) \sim \mathcal{CN}(0, \mathbf{Q}_m)$. Assuming that both the looks and the backscattering sources are independent, the vectors $\mathbf{x}_i(n_1)$ and $\mathbf{x}_l(n_2)$ are mutually independent for $i \neq l$, or $n_1 \neq n_2$. We also assume that the speckle correlation sequences, $r_{xm}(k)$, are real valued. This implies that the spatial spectra of the speckle components are symmetric around zero frequency. Note that we have assumed that the covariance matrix may change from one source to the other, but it does not depend on the look index n, i.e., for each m the vectors $\{x_m(n)\}_{n=1}^N$ are independent and identically distributed (IID). This is a common assumption in SAR processing [2]. Finally, $\{\mathbf{v}(n)\}$ are N IID complex white Gaussian distributed vectors

whose components have power σ_v^2. The problem of interest here is the estimation of the radar reflectivities $\{\tau_m\}_{m=1}^{N_s}$, from the observed $\{\mathbf{y}(n)\}_{n=1}^{N}$, with unknown $\{\varphi_m\}_{m=1}^{N_s}$, $\{\mathbf{Q}_m\}_{m=1}^{N_s}$, σ_v^2, and array uncertainty as in (3).

III. MULTILOOK STANDARD CAPON BEAMFORMER

Let $\mathbf{h}_\varphi$ be a K-dimensional spatial Capon filter designed such that (see, e.g., [12])

$$\min_{\mathbf{h}_\varphi} \mathbf{h}_\varphi^H \mathbf{R}_y \mathbf{h}_\varphi \qquad \text{subject to} \quad \mathbf{h}_\varphi^H \bar{\mathbf{a}}(\varphi) = 1. \tag{14}$$

Assuming that the inverse of $\mathbf{R}_y$ exists, the filter minimizing (14) is obtained as

$$\mathbf{h}_\varphi = \frac{\mathbf{R}_y^{-1}\bar{\mathbf{a}}(\varphi)}{\bar{\mathbf{a}}^H(\varphi)\mathbf{R}_y^{-1}\bar{\mathbf{a}}(\varphi)} \tag{15}$$

yielding the estimated power of the filter output

$$\hat{\sigma}^2_{\text{MSCB}}(\varphi) = \mathbf{h}_\varphi^H \mathbf{R}_y \mathbf{h}_\varphi = \frac{1}{\bar{\mathbf{a}}^H(\varphi)\mathbf{R}_y^{-1}\bar{\mathbf{a}}(\varphi)}. \tag{16}$$

The estimated power yields the interferometric phase estimates $\hat{\varphi}_m$ as the locations of the N_s highest peaks in the spectrum; the reflectivities are then estimated as [15]

$$\hat{\tau}_m = \frac{1}{N}\sum_{n=1}^{N} |\hat{\alpha}_m(n)|^2, \qquad \text{for} \quad m = 1,\ldots,N_s \tag{17}$$

where $\hat{\alpha}_m(n)$ are the least-squares estimates of the complex amplitudes of cisoids for the nth look, i.e.,

$$\hat{\boldsymbol{\alpha}}(n) = (\mathbf{A}^H\mathbf{A})^{-1}\mathbf{A}^H\mathbf{y}(n) \tag{18}$$

where

$$\hat{\boldsymbol{\alpha}}(n) = [\hat{\alpha}_1(n) \quad \ldots \quad \hat{\alpha}_{N_s}(n)]^{\mathrm{T}} \tag{19}$$

$$\mathbf{A} = [\bar{\mathbf{a}}(\hat{\varphi}_1) \quad \ldots \quad \bar{\mathbf{a}}(\hat{\varphi}_{N_s})]. \tag{20}$$

In practice, $\mathbf{R}_y$ is unknown and must be estimated from the data. As was shown in [20], one often obtain improved spectral estimates by using the forward-backward averaged sample covariance matrix,

$$\hat{\mathbf{R}}_y = \frac{1}{2}(\hat{\mathbf{R}}_f + \mathbf{J}\hat{\mathbf{R}}_f^{\mathrm{T}}\mathbf{J}) \tag{21}$$

where $\mathbf{J}$ is the $K \times K$ exchange matrix, and

$$\hat{\mathbf{R}}_f = \frac{1}{N}\sum_{n=1}^{N} \mathbf{y}(n)\mathbf{y}^H(n). \tag{22}$$

In the following, we refer to the power estimate obtained from (17), using (21), as the MSCB. Note that if $N < K$, the inverse of $\hat{\mathbf{R}}_y$ will not exist, posing a lower bound on the number of looks that needs to be acquired to evaluate (16). This requirement can to some extent be relaxed by instead using the RCB introduced in [16].

IV. MULTILOOK ROBUST CAPON BEAMFORMER

Following [16], we rewrite (14) as

$$\max_{\sigma^2(\varphi),\mathbf{a}(\varphi)} \sigma^2(\varphi)$$

$$\text{subject to} \quad \mathbf{R}_y - \sigma^2(\varphi)\mathbf{a}(\varphi)\mathbf{a}^H(\varphi) \geq 0 \tag{23}$$

for any $\mathbf{a}(\varphi)$ satisfying (3). Here, $\sigma^2(\varphi)$ denotes the power corresponding to the interferometric phase φ, and the notation $\mathbf{P} \geq 0$ (for any Hermitian matrix $\mathbf{P}$) means that $\mathbf{P}$ is positive semidefinite. As described in [17], (23) can be reformulated as

$$\min_{\mathbf{a}(\varphi)} \mathbf{a}^H(\varphi)\mathbf{R}_y^{-1}\mathbf{a}(\varphi) \qquad \text{subject to} \quad (3) \tag{24}$$

which, by introducing

$$\mathbf{C}^{-1} = \frac{1}{\epsilon}\mathbf{D}^H\mathbf{D} \quad \Rightarrow \quad \mathbf{D} = \sqrt{\epsilon}\mathbf{C}^{-1/2} \tag{25}$$

for some $\epsilon > 0$, can be rewritten as

$$\min_{\tilde{\mathbf{a}}(\varphi)} \tilde{\mathbf{a}}^H(\varphi)\tilde{\mathbf{R}}_y^{-1}\tilde{\mathbf{a}}(\varphi)$$

$$\text{subject to} \quad \|\tilde{\mathbf{a}}(\varphi) - \tilde{\bar{\mathbf{a}}}(\varphi)\|^2 \leq \epsilon \tag{26}$$

where $\tilde{\mathbf{a}}(\varphi) = \mathbf{D}\mathbf{a}(\varphi)$, $\tilde{\bar{\mathbf{a}}}(\varphi) = \mathbf{D}\bar{\mathbf{a}}(\varphi)$ and $\tilde{\mathbf{R}}_y = \mathbf{D}\mathbf{R}_y\mathbf{D}^H$. As was shown in [17], this minimization can be efficiently solved using the Lagrange multiplier methodology, minimizing

$$f = \tilde{\mathbf{a}}^H(\varphi)\tilde{\mathbf{R}}_y^{-1}\tilde{\mathbf{a}}(\varphi) - \lambda(\|\tilde{\mathbf{a}}(\varphi) - \tilde{\bar{\mathbf{a}}}(\varphi)\|^2 - \epsilon) \tag{27}$$

where λ is the Lagrange multiplier. Let

$$\mathbf{R}_y = \mathbf{U}\boldsymbol{\Gamma}\mathbf{U}^H \tag{28}$$

where the columns of $\mathbf{U}$ contain the eigenvectors of $\mathbf{R}_y$, and the diagonal elements of $\boldsymbol{\Gamma}$ the corresponding eigenvalues. Then, the minimum of (27), over λ, yields an estimate of the actual array steering vector (see [17] for further details)

$$\hat{\tilde{\mathbf{a}}}(\varphi) = \tilde{\bar{\mathbf{a}}}(\varphi) - \mathbf{U}(\mathbf{I} + \lambda\boldsymbol{\Gamma})^{-1}\mathbf{U}^H\tilde{\bar{\mathbf{a}}}(\varphi). \tag{29}$$

We refer to the estimated reflectivities, obtained by using the above estimated steering vector in the least-squares estimates in (17) and (20), using (21), as the MRCB. Here, the interferometric phase estimates $\hat{\varphi}_m$ are obtained as the locations of the N_s highest peaks in the reflectivity spectrum in (17).

V. NUMERICAL EXAMPLE

Performance analysis has been carried out assuming that the vectors $\{\mathbf{x}_m(n)\}_{n=1}^{N}$ are IID with zero mean and spatial autocorrelation sequence given

by

$$r_{xm}(k) = \mathrm{E}\{[\mathbf{x}_m(n)]_l \cdot [\mathbf{x}_m(n)]^*_{l+k}\} = \begin{cases} 1 - \dfrac{|k|}{K-1} b_m, & \text{for} \quad |k| \le \dfrac{K-1}{b_m} \\ 0, & \text{otherwise} \end{cases} \tag{30}$$

where $(\cdot)^*$ denotes conjugate, K is the number of phase centers in the InSAR system and $b_m = B/B_{cm}$ is the normalized baseline relative to the mth patch, with B_{cm} denoting the critical baseline, i.e., the space separation for which the mth speckle term considered in isolation is completely decorrelated at the extremities of the array; it depends on the radar system parameters and on the local slope of the mth patch [1]. This triangular correlation sequence is the basic speckle model used in SAR interferometry for flat extended targets [1, 2]. Throughout these simulations, we assume a case with two sources present ($N_s = 2$). The choice of K in practical systems/champaigns is a trade-off among cost, Rayleigh resolution along the elevation angle, unambiguous height range, and possible temporal decorrelation in repeat-pass systems. Here, generally $K = 8$ is adopted as an average value representative of both airborne and spaceborne existing or planned systems [4, 5, 7, 21–23], but we also examine how the methods work for other number of phase centers. Furthermore, we assume that the values of the parameters are: $\varphi_1 = 0°$, $\varphi_2 = 540°$, $N = 32$, $b_1 = b_2 = 0.2$, $\mathrm{SNR}_1 = \mathrm{SNR}_2 = 12$ dB, where SNR_m is the signal-to-noise ratio of the mth source, defined as $\mathrm{SNR}_m = \tau_m/\sigma_v^2$. Two sources with normalized baselines b_1 and b_2 are considered adjacent when $\Delta\varphi = |\varphi_1 - \varphi_2|$ is equal to $\Delta\varphi_{ad} = 2\pi(b_1 + b_2)$. When separated less than $\Delta\varphi_{ad}$, the sources collapse into only one [15]. In our case, the Rayleigh resolution limit is $\Delta\varphi_B = 2\pi(K-1)/K = 315°$, and $\Delta\varphi_{ad} = 144°$, so $\Delta\varphi \gtrapprox \Delta\varphi_B > \Delta\varphi_{ad}$. The performance of the estimators is analyzed in terms of normalized root mean square error (RMSE),

$$\mathrm{RMSE}(\hat{\tau}_m) = \sqrt{E\{(\hat{\tau}_m - \tau_m)^2\}}/\tau_m \tag{31}$$

evaluated by means of 10^3 Monte-Carlo simulations. Figs. 2 and 3 show the RMSE of the second reflectivity estimates (the other behaves similarly) for varying perturbation levels, $\sigma^2_{i\perp B}$ and $\sigma^2_{i\parallel B}$. As seen from the figures, the MRCB is yielding preferable estimates for both frontal and transverse perturbations as compared with the MSCB and the beamformer. Here, when generating the data, we have used the approximate steering vector in (8), with the perturbations added as random Gaussian noise. In these figures, only one of the perturbations has been varied, with the other being set to zero; $\mathbf{C}$ is set

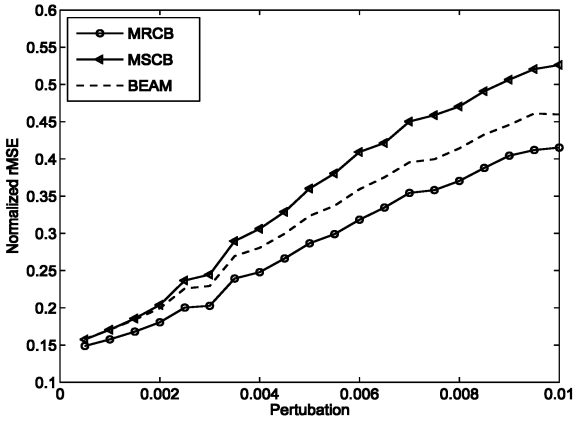

Fig. 2. RMSE of reflectivity estimates of second source versus transverse perturbation $\sigma^2_{i\perp B}$.

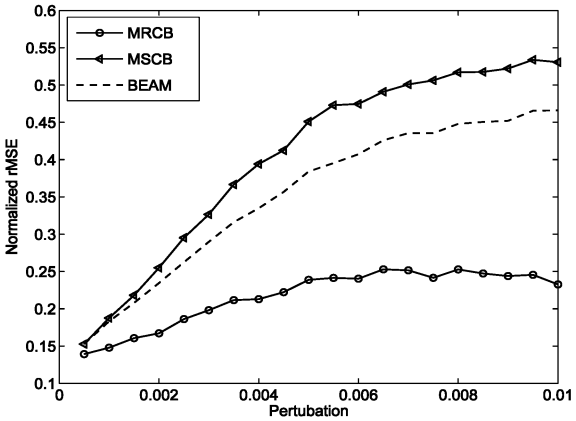

Fig. 3. RMSE of reflectivity estimates of second source versus frontal perturbation $\sigma^2_{i\parallel B}$.

according to the worst case value given in (12), with $\varphi_{\max} = \varphi_2$, and as a result $\mathbf{D} = \mathbf{I}$. Typically, the level of these perturbations are not a priori perfectly known, and cannot be used to give more than an approximate value of $\epsilon \approx \mathrm{var}_{\max}\{[\mathbf{e}_a(\varphi_m)]_i\}$. Fortunately, the MRCB is robust to the choice of ϵ as well [17], i.e., the method is robust to the impact of an mismatch between the assumed and the actual perturbations. This robustness is seen in Fig. 4, where the RMSE is shown as a function of multiples of ϵ; here, both $\sigma^2_{i\perp B} = \sigma^2_{i\parallel B} = 0.002$ implying $\epsilon = 0.32$, but as seen in the figure the choice of ϵ can be allowed to vary over a large range of values without significantly affecting the quality of the estimates. However, the choice of ϵ will determine the search range for λ used in the minimization in (27) [17]; in our experience, due the approximative nature of $\mathrm{var}_{\max}\{[\mathbf{e}_a(\varphi_m)]_i\}$, it is often better to allow for a somewhat larger search range over λ than what is proposed in [17]. In these simulations, we have allowed λ a 5 times larger search range, extending the allowed upper limit of λ, as compared with the one used in [17]. Further, we examine how a minor perturbation will affect the performance of the different estimators.

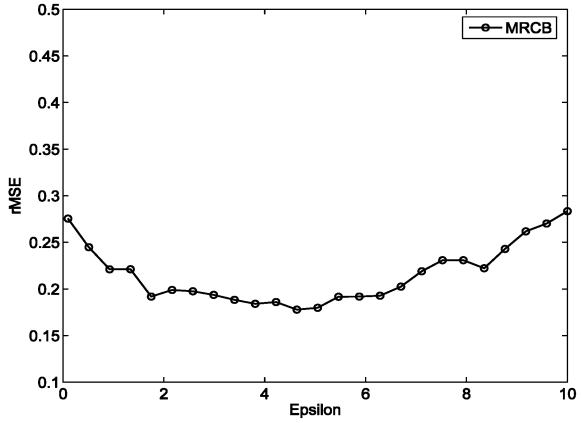

Fig. 4. RMSE of reflectivity estimates of second source versus multiples of ε.

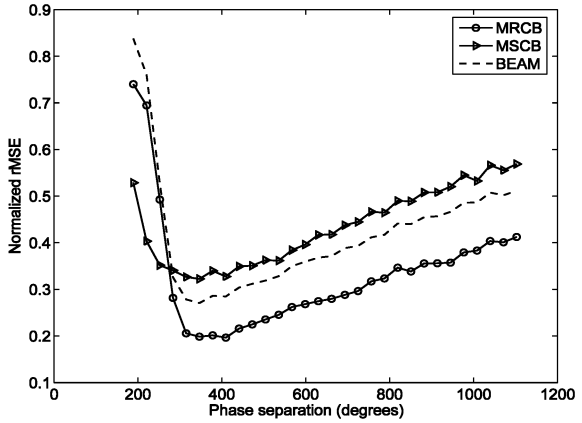

Fig. 5. RMSE of reflectivity estimates of second source versus interferometric phase separation $\Delta\varphi$.

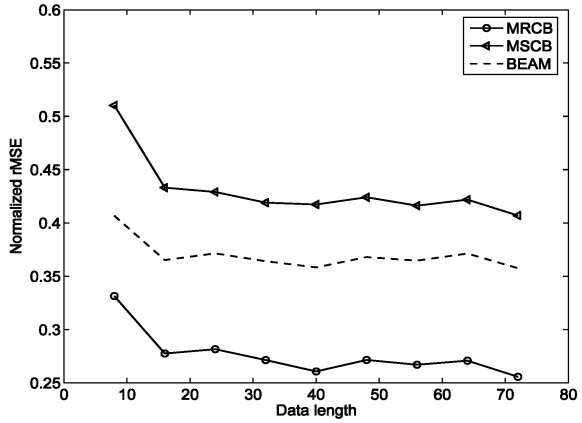

Fig. 6. RMSE of reflectivity estimates of second source versus number of looks N.

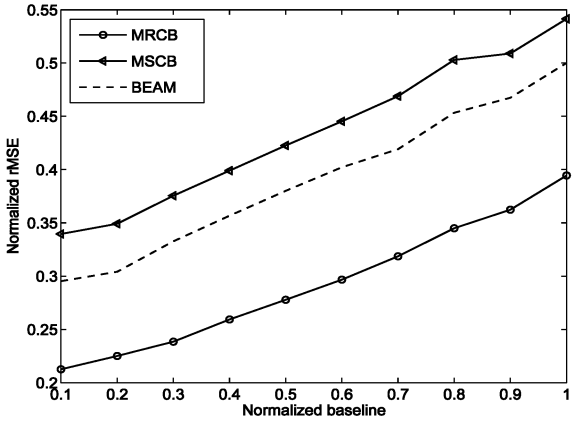

Fig. 7. RMSE of reflectivity estimates of second source versus its normalized baseline b_2.

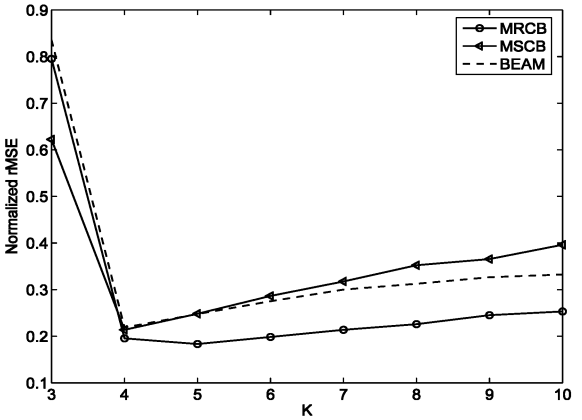

Fig. 8. RMSE of reflectivity estimates of second source versus number of phase centers K.

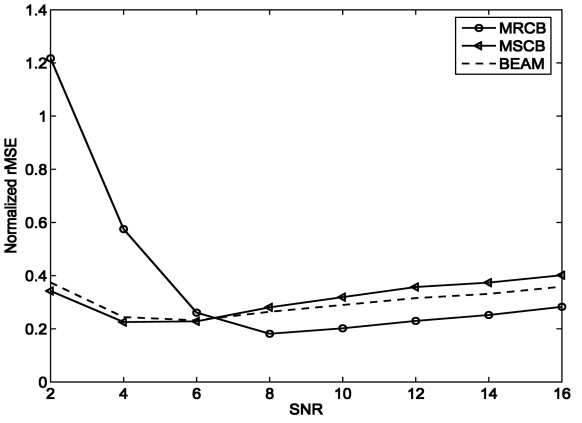

Fig. 9. RMSE of reflectivity estimates of second source versus its SNR, SNR_2.

Figs. 5–9 show the RMSE of the second reflectivity estimates for varying interferometric phase separation, number of looks (N), normalized baseline (b_2), number of phase centers (K), and SNR. Here, $\sigma^2_{i\perp B} = \sigma^2_{i\|B} = 0.002$. As shown in Fig. 5, it is apparent how the conventional beamformer degrades beyond the Rayleigh resolution limit, and how the proposed MRCB generally performs better than both the beamformer and MSCB; the price paid is a somewhat lower resolution for the MRCB as compared with the MSCB, although the resulting resolution is still preferable as compared with the beamformer. Figs. 6–8 indicate that also for low number of looks, in the presence of widely extended targets, and for low number of phase centers, the robustness property of the proposed MRCB is retained. However, it is worth noting that the MRCB will not always yield preferable estimates; Fig. 9 shows how the advantage

of MRCB is lost when the SNR of the second peak is much weaker than the first peak. In such cases, the MRCB is not able to locate the weaker peak, and the method fails to provide reliable estimates.

VI. CONCLUSIONS

In this work, we applied the recent RCB in the multibaseline InSAR scenario introducing an array error model for this specific application. Moreover, we also extended the robust approach to the least squares estimator of the signal amplitudes. We found that when array errors are present, the performance of the robust Capon method is often preferable to both the standard Capon and the beamforming approaches.

ACKNOWLEDGMENT

The authors are grateful to Professor Jian Li, Professor Petre Stoica and Mr. Zhisong Wang for providing us with their efficient implementation of the RCB.

ANDREAS JAKOBSSON
Dept. of Electrical Engineering
Karlstad University
SE-651 88 Karlstad
Sweden
E-mail: (andreas.jakobsson@ieee.org)

FULVIO GINI
FABRIZIO LOMBARDINI
Dept. of Ingegneria
dell'Informazione
University of Pisa
Via Diotisalvi 2
I-56126 Pisa
Italy

REFERENCES

[1] Rodriguez, E., and Martin, J. M.
Theory and design of interferometric synthetic aperture radar.
Proceedings of IEE, Pt. F, **139** (Apr. 1992), 147–159.

[2] Henderson, F. M., and Lewis, A. J.
Manual of Remote Sensing, Vol. 2, Principles and Applications of Imaging Radar (3rd ed.).
New York: John Wiley and Sons, Inc., 1998.

[3] Homer, J., Longstaff, I. D., and Callaghan, G.
High resolution 3-D SAR via multi-baseline interferometry.
In *Proceedings of the IEEE International Geoscience and Remote Sensing Symposium*, Lincoln, NB, 1996, 796–798.

[4] Roessing, L., and Ender, J. H. G.
Multi-antenna SAR tomography using superresolution techniques.
In *3rd European Conference on Synthetic Aperture Radars*, Munich, Germany, May 23–25, 2000, 55–58.

[5] She, Z., Gray, D. A., Bogner, R. E., and Homer, J.
Three-dimensional SAR imaging via multiple pass processing.
In *Proceedings of the IEEE International Geoscience and Remote Sensing Symposium*, Hamburg, Germany, 1999, 2389–2391.

[6] Xiao, S., and Munson, D. C.
Spotlight-mode SAR imaging of a three-dimensional scene using spectral estimation techniques.
In *Proceedings of the IEEE International Geoscience and Remote Sensing Symposium*, Seattle, WA, 1998, 642–644.

[7] Reigber, A., and Moreira, A.
First demonstration of airborne SAR tomography using mulitbaseline L-band data.
IEEE Transactions on Geoscience and Remote Sensing, **38** (Sept. 2000), 2142–2152.

[8] Berardino, P., Fornaro, G., Lanari, R., Sansosti, E., Serafino, F., and Soldovieri, F.
Multi-pass synthetic aperture radar for 3-D focusing.
In *2002 IEEE International Geoscience and Remote Sensing Symposium*, Toronto, Canada, 2002, 176–178.

[9] Corsini, G., Diani, M., Lombardini, F., and Pinelli, G.
Simulated analysis and optimization of a three-antenna airborne InSAR system for tomographic mapping.
IEEE Transactions on Geoscience and Remote Sensing, **37**, 5 (1999), 2518–2529.

[10] Jakobsson, A., Lombardini, F., and Gini, F.
Weighted subspace fitting of interferometric phases for multibaseline SAR interferometry.
In *Proceedings of Seventh International Symposium on Signal Processing and its Applications*, Paris, July 1–4, 2003.

[11] Gini, F., and Lombardini, F.
Multilook APES for multibaseline SAR interferometry.
IEEE Transactions on Signal Processing, **50** (July 2002), 1800–1803.

[12] Gini, F., Lombardini, F., and Montanari, M.
Layover solution in multibaseline SAR interferometry.
IEEE Transactions on Aerospace and Electronics Systems, **38** (Oct. 2002), 1344–1356.

[13] Cox, H.
Resolving power and sensitivity to mismatch of optimum array processors.
Journal of the Acoustical Society of America, **54** (Sept. 1973), 771–785.

[14] Oliver, C., and Quegan, S.
Understanding Synthetic Aperture Radar Images.
Norwood, MA: Artech House, 1998.

[15] Lombardini, F., Montanari, M., and Gini, F.
Reflectivity estimation for multibaseline interferometric radar imaging of multiple extended sources.
IEEE Transactions on Signal Processing, **51** (June 2003), 1508–1519.

[16] Stoica, P., Wang, Z., and Li, J.
Robust capon beamforming.
IEEE Signal Processing Letters, **10** (June 2003), 172–175.

[17] Li, J., Stoica, P., and Wang, Z.
On robust capon beamforming and diagonal loading.
IEEE Transactions on Signal Processing, **51** (July 2003), 1702–1715.

[18] Gini, F., and Bordoni, F.
On the behaviour of information theoretic criteria for model order selection of InSAR signals corrupted by multiplicative noise.
Signal Processing, **83** (2003), 1047–1063.

[19] Gini, F., Lombardini, F., and Verrazzani, L.
On the implementation of ITC methods for model order selection into multibaseline InSAR systems.
Presented at 2003 Tyrrhenian International Workshop on Remote Sensing, Elba Island, Italy, 2003.

[20] Jansson, M., and Stoica, P.
Forward-only and forward-backward sample covariances—A comparative study.
Signal Processing, **77**, 3 (1999), 235–245.

[21] Ender, J. H. G., and Brenner, A. R.
PAMIR—A wideband phased array SAR/MTI system.
In *Proceedings of 4th European Conference on Synthetic Aperture Radar*, Cologne, Germany, June 2002, 157–162.

[22] Ferretti, A., Guarnieri, A. M., Prati, C., and Rocca, F.
Multi-baseline interferometric techniques and applications.
In *FRINGE '96—ESA Workshop*, Zurich, Switzerland, 1996, 243–252.

[23] Ramongassie, S., Phalippou, L., Thouvenot, E., and Massonet, D.
Preliminary design of the payload for the interferometric cartwheel.
In *Proceedings of the 3rd European Conference on Synthetic Aperture Radar*, Munich, Germany, May 2000, 29–32.

Aeronautical Telemetry using Offset QPSK in Frequency Selective Multipath

The impact of frequency selective multipath fading on the bit error rate performance of ARTM Tier-1 waveforms (FQPSK and SOQPSK) is derived and analyzed. In the presence of a strong specular reflection with relative magnitude $|\Gamma_1|$, the ARTM Tier-1 waveforms suffer a loss in performance of $(1-|\Gamma_1|)^{-4\sqrt{|\Gamma_1|}}$ for $|\Gamma_1|<0.5$ and a relatively high error floor at approximately 10^{-2} for $|\Gamma_1|\geq 0.5$. The ARTM Tier-1 waveforms possess twice the spectral efficiency of PCM/FM, but exhibit a greater loss and higher error floors than PCM/FM for the same multipath conditions and signal-to-noise ratio.

I. INTRODUCTION

Pulse-code modulation (PCM)/FM has been the primary modulation format used in aeronautical telemetry for more than 40 years. During this time, the complexity of the systems that are tested has increased dramatically. As a consequence the required data rates for the tests have increased from 100 kbits/s in the early 1970s to 10–20 Mbit/s today. This increase has applied tremendous pressure on the spectrum allocated to aeronautical telemetry at L-band (1435–1535 MHz), lower S-band (2200–2290 MHz), and upper S-band (2310–2390 MHz). The situation was further exacerbated in 1997 when the lower portion of upper S-band from 2310 to 2360 MHz was reallocated in two separate auctions.[1]

In response to these trends, the Advanced Range Telemetry (ARTM) program [1] was launched by the Central Test and Evaluation Investment Program (CTEIP) in 1997 to identify more bandwidth-efficient modulation formats compatible with fully saturated nonlinear amplifiers used in aeronautical telemetry. Modulation formats with improved spectral efficiency were selected in two phases. In the first phase, Feher-patented quadrature phase-shift keying (QPSK) (FQPSK) [2] and a compatible variant of the MIL-STD 188-181 shaped offset QPSK (SOQPSK) [3] were selected. These two modulation formats, known collectively as "ARTM Tier-1 waveforms," have twice the spectral efficiency as PCM/FM [4], even when used with nonlinear power amplifiers.

As the data rates used for aeronautical telemetry have increased, the multipath interference has become increasingly frequency selective and has proven to be the dominant channel impairment. A model for the multipath in aeronautical telemetry is described in [5] where it was shown that the dominant feature is a "ground bounce" with complex amplitude Γ_1 and delay τ_1. The effect of frequency selective multipath interference on PCM/FM was analyzed in [6] where it was shown that the loss in bit error rate performance (relative to the additive white Gaussian noise (AWGN)-only environment) is bounded by $(1-|\Gamma_1|)^{-2|\Gamma_1|}$.

In the work presented here, we analyze the effect of frequency selective multipath on the ARTM Tier-1 waveforms. We show that in the presence of a strong specular multipath reflection with magnitude $|\Gamma_1|$, the loss in performance for FQPSK is $(1-|\Gamma_1|)^{-4\sqrt{|\Gamma_1|}}$ for $|\Gamma_1|<0.5$. An error floor at approximately 10^{-2} occurs for $|\Gamma_1|\geq 0.5$. A performance analysis of FQPSK is described in Section II and numerical results are presented in Section III. The relationship between FQPSK and SOQPSK is discussed in Section IV. Conclusions are presented in Section V.

II. PERFORMANCE ANALYSIS

A. Mathematical Description of FQPSK

FQPSK [7] is a variant of offset QPSK where the inphase and quadrature components of the modulated waveform are cross correlated to produce a quasi-constant envelope signal [8], [9]. Following Simon [9], the FQPSK waveform may be expressed in terms of a set of 16 baseband pulse shapes $S_m(t)$

Manuscript received March 1, 2004; revised October 15, 2004; released for publication November 26, 2004.

IEEE Log No. T-AES/41/2/849052.

Refereeing of this contribution was handled by T. F. Roome.

This work was supported by T&E S&T Spectrum Efficient Technologies Program under U.S. Air Force Grant DOD ARTM F04611-02-C-0020.

[1] 2320–2345 MHz was reallocated for digital audio radio in one auction while 2305–2320 MHz and 2345–2360 MHz were allocated to wireless communications services in the other auction.